PNAS RESEARCH ARTICLE | APPLIED BIOLOGICAL SCIENCES APPLIED PHYSICAL SCIENCES OPEN ACCESS

Hybrid measurement of respiratory aerosol reveals a dominant coarse fraction resulting from speech that remains airborne for minutes

Yang Shen[a,1], Joseph M. Courtney[a,1], Philip Anfinrud[a], and Adriaan Bax[a,2]

Edited by Axel Brunger, Stanford University, Stanford, CA; received February 19, 2022; accepted April 27, 2022

Accurate measurements of the size and quantity of aerosols generated by various human activities in different environments are required for efficacious mitigation strategies and accurate modeling of respiratory disease transmission. Previous studies of speech droplets, using standard aerosol instrumentation, reported very few particles larger than 5 μm. This starkly contrasts with the abundance of such particles seen in both historical slide deposition measurements and more recent light scattering observations. We have reconciled this discrepancy by developing an alternative experimental approach that addresses complications arising from nucleated condensation. Measurements reveal that a large volume fraction of speech-generated aerosol has diameters in the 5- to 20-μm range, making them sufficiently small to remain airborne for minutes, not hours. This coarse aerosol is too large to penetrate the lower respiratory tract directly, and its relevance to disease transmission is consistent with the vast majority of severe acute respiratory syndrome coronavirus 2 (SARS-CoV-2) infections initiating in the upper respiratory tract. Our measurements suggest that in the absence of symptoms such as coughing or sneezing, the importance of speech-generated aerosol in the transmission of respiratory diseases is far greater than generally recognized.

airborne lifetime | COVID-19 | speech droplet | respiratory droplet | virus transmission

Respiratory tract infections are caused by a wide range of pathogenic organisms (1), including a large array of respiratory viruses, such as influenza virus, rhinovirus, measles virus, respiratory syncytial virus, adenovirus, and most recently, severe acute respiratory syndrome coronavirus 2 (SARS-CoV-2). In all these diseases, person-to-person spread involves respiratory droplets, which originate from the mucus layer that covers the epithelium of the respiratory tract or from oral fluid present in the mouth, mostly as saliva. Thus, characterizing respiratory droplets is essential to understanding respiratory pathogen transmission and will inform effective public health policies to curb infections. Four mechanisms for droplet generation are generally considered: breathing, speaking (singing, laughing, etc.), coughing, and sneezing (2). Considering the well-recognized importance of asymptomatic transmission of SARS-CoV-2 (3), our study focuses on the first two of these mechanisms.

As highlighted by Wells (4) and Duguid (2) nearly a century ago, the vast majority of respiratory droplets are smaller than ca. 100-μm diameter and fully dehydrate once entering the atmosphere. These desiccated droplets can remain airborne for minutes to hours before landing on solid surfaces. If generated by a person infected by a respiratory virus, they will contain virions that can remain viable and infectious for many hours (5, 6). Upon inhalation, airborne particles can reach different parts of the respiratory tract depending on their size: coarse aerosols with diameter $D \gtrsim 5$ μm (7) deposit in the upper respiratory tract (URT), and fine aerosols with $D < 5$ μm can penetrate deep into the lower respiratory tract (LRT). Many viral pathogens, including SARS-CoV-2, influenza, rhinovirus, and measles virus, can infect both URT and LRT epithelia (1, 8, 9), with URT infections typically associated with mild initial symptoms and LRT infections possibly resulting in life-threatening pneumonia (1, 10–13). Direct infection of the LRT, before the adaptive immune system has been triggered by vaccination or a preceding URT infection, presents a greater risk.

An URT infection also can expand into the LRT through microaspiration of oropharyngeal fluids (14, 15). The extent to which inhalation of self-generated URT cough, speech, or sneeze aerosols may contribute to this migration remains unknown. However, it has been argued that this pathway could be significant because an infected carrier is invariably at the center of their own speech aerosol cloud, which results in strongly elevated exposure (16). The risk of migration from the URT to the LRT rises with the viral load and the viability of the virus, which peak around and just prior to

Significance

Respiratory droplets are widely recognized as the primary vehicle in viral respiratory disease transmission. Accurate information on their number and size distributions is important for appropriate mitigation strategies, for quantitative modeling of airborne disease transmission, and for evaluating the relative importance of droplets originating from saliva versus airway lining fluid. A straightforward experimental setup using inexpensive, readily available components is developed for simultaneous characterization of larger particles by video analysis of laser light scattering and monitoring of smaller sizes by an optical particle counter. Measurements indicate that in a healthy volunteer, the airborne mass of speech aerosol far exceeds that generated by breathing, even when accounting for faster sedimentation of the larger particles.

Author affiliations: [a]Laboratory of Chemical Physics, National Institute of Diabetes and Digestive and Kidney Diseases (NIDDK), NIH, Bethesda, MD 20892-0520

Author contributions: P.A. and A.B. designed research; Y.S., J.M.C., and A.B. performed research; Y.S. and J.M.C. analyzed data; and P.A. and A.B. wrote the paper.

The authors declare no competing interest.

This article is a PNAS Direct Submission.

[1]Y.S. and J.M.C. contributed equally to this work.

[2]To whom correspondence may be addressed. Email: bax@nih.gov.

This article contains supporting information online at http://www.pnas.org/lookup/suppl/doi:10.1073/pnas.2203086119/-/DCSupplemental.

Published June 21, 2022.

the onset of symptoms, respectively (17, 18). For the original Wuhan strain of the SARS-CoV-2 virus, the onset of symptoms occurs about 5 days after the initial infection (17, 19), but it occurs somewhat earlier for the more infectious delta and omicron variants (20).

To evaluate the risk of LRT infection, it is important to know the size distribution of particles generated by various respiratory activities. For talking, coughing, and sneezing, studies historically relied on slide sampling techniques of increasing sophistication, followed by microscope observation (2, 21, 22). Droplets generated by breathing or vowel sounds are numerous but very small ($\lesssim$2 μm) and thus more difficult to evaluate with those classical methods. Instead, such small droplets are now commonly quantified by aerosol detection equipment, such as optical particle sizers (OPSs), based on light scattering (22, 23); aerodynamic particle sizers (APSs), based on the time-of-flight measurement in an accelerating flow field (24); and scanning mobility particle sizers that derive a particle's size from its mobility in an electric field and are best suited for very small sizes ($\lesssim$1 μm) (25, 26). APS instruments are less efficient at detecting medium-sized liquid particles, and undercounts as high as 75% for 10-μm droplets have been reported (27).

There is some confusion in the literature about the hydration state of reported sizes of respiratory aerosol particles, which shrink by a factor of γ upon evaporation of their aqueous content, thus by a factor of γ^3 in volume. After full dehydration, a particle's radius is determined by its amount of nonvolatile matter. Estimates for γ vary substantially: Nicas et al. (28) proposed $\gamma = 2$ for breath particles, based on data extracted from breath condensate by Effros et al. (29) that indicated a high fraction (ca. 8% wt/vol) of glycoproteins, presumably mucins. Holmgren et al. (30) reported $\gamma = 2.4$ for breath particles when the relative humidity (RH) is reduced from 99.5% in the small airways to 75%. Bagheri et al. (26) observed $\gamma = 4.5$ for singing particles in a diffusion dryer or $\gamma = 4$ for large saliva droplets observed directly by microscope imaging. Some of those measurements were conducted directly at the mouth opening, observing the hydrated state using light scattering or holographic imaging techniques (26, 31). Clearly, the concentration of pathogens in dehydrated particles scales with γ^3 relative to the originating airway lining fluid (ALF) or saliva. However, the high uncertainty in the applicable γ value, which is frequently not even reported, prevents accurate estimates of airborne virus concentrations.

Recently, we and others demonstrated that speech particles can be readily observed by simple video recordings of light scattering by these particles (32–35). Such recordings not only present a visually compelling warning to the public but also provide opportunities to monitor particles before, during, and after dehydration. Those light scattering measurements focused on particles larger than a few microns due to technical sensitivity issues. The intensity of scattered light scales with the square of a particle's diameter, causing a dynamic range problem and rendering it more challenging to observe the smallest particles, especially in the presence of larger particles. Inexpensive, fast consumer cameras typically use 10- to 12-bit analog-to-digital converters (ADCs), thereby limiting dynamic range; while detectors with an increased ADC range are available, their speed is often insufficient for high-speed recording.

Here, we aim to evaluate the entire range of speech droplet sizes produced during different breathing and speaking protocols. To do so, we combined video-recorded light scattering and an OPS to evaluate droplets from 0.3 to 100 μm. Our data show a continuous spectrum that lacks previously reported gaps in the size distribution (36). Our measurements confirm that the gravitational settling rate for dehydrated particles larger than 5 μm steeply increases with size, but considering the high numbers, volumes, and airborne lifetimes of those particles, they are likely to be a dominant factor in transmission of disease.

Results

Because the aerosol concentration found indoors typically greatly exceeds that of respiratory particles, either all measurements needed to be carried out in a cleanroom or subjects needed to clean their lungs by breathing through a high-quality, high-efficiency particulate air (HEPA) filter for at least a minute prior to measurements. The latter method was used for all our work.

Nucleated Condensation. When water-saturated air exits the mouth ~35 °C and thermally equilibrates with cooler, ambient air, the RH surrounding emitted droplets can exceed 100%, which leads to nucleated condensation and a rapid increase in droplet size. As the RH of the expired air equilibrates with the ambient air, droplet growth terminates, and droplets subsequently shrink to their desiccated size. The temporary mass increase, caused by nucleated condensation, accelerates gravitational sedimentation, which can interfere with travel of the particle into traditional aerosol detection equipment and produce a steep, size-dependent drop in its detection efficiency. This effect may explain the particle count discrepancy between studies employing particle counters and those based upon microscope slide deposition. However, decreased efficiency of APS instruments in detecting larger liquid particles will also play a role (27).

Our video recording of light scattered by expired air crossing a 0.7-mm-thick sheet of bright light indicates a very large number ($>10^5$ per liter) of breath droplets (Fig. 1), despite a detection threshold of ca. 1 μm. Here, due to nucleated condensation, droplets whose scattering power would otherwise be below the detection threshold have grown to sizes that are detectable. These observations contrast with prior measurements of breath droplets from healthy volunteers, which showed ca. 100 particles per liter during normal, tidal breathing, with the vast majority ($\gtrsim$80%) of dehydrated diameters smaller than 1 μm (27, 37, 38).

For our present recordings, the exhaled air enters the observation chamber through a carbon-fiber tube that terminates ca. 7 cm before the light sheet (*Materials and Methods*), and nucleated condensation can occur during the entire travel time (ca. 0.5 s) within the tube. The speed at which a particle grows (or shrinks) under nonequilibrium conditions scales inversely with its radius (39). Thus, smaller particles grow faster than larger ones, resulting in droplets with relatively homogeneous brightness (Fig. 1). However, when the temperature of the chamber and carbon-fiber tube was raised to ca. 32 °C, nucleated condensation vanished and the observed particle counts drop to $\lesssim$100 per liter, consistent with prior measurements (27, 37, 38).

Collecting Aerosols. The vast majority of prior studies aimed to detect respiratory aerosols in real time, i.e., synchronous with the time at which they were generated. However, because the time needed for dehydration scales with the square of a particle's initial D, it becomes challenging to detect particles at a well-defined hydration state over a wide range of sizes. Here, we overcome that limitation by first injecting a short burst of droplets into a low-humidity chamber, where they desiccate before settling to the floor of the chamber. This simple and

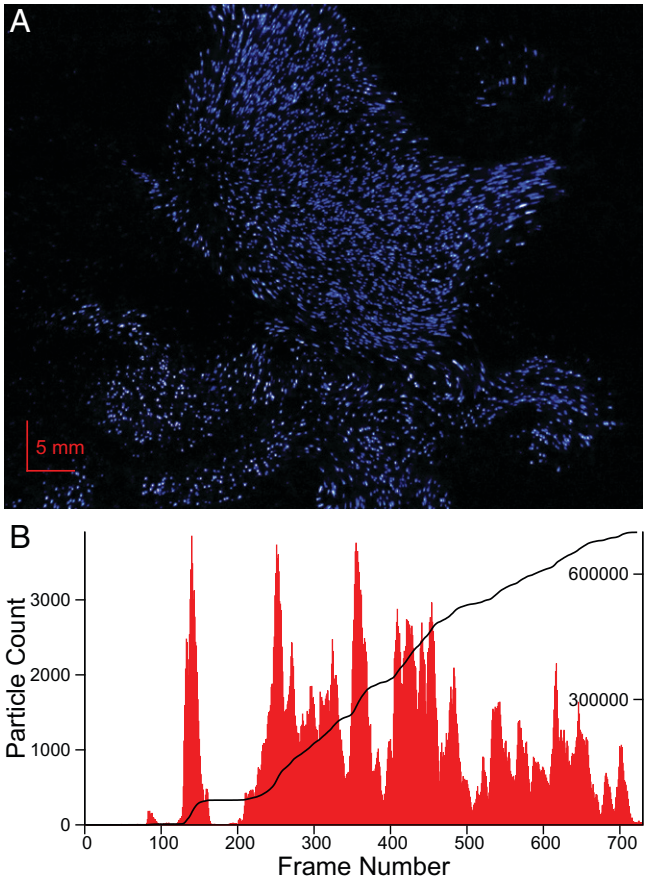

Fig. 1. Video recording of laser light scattered by breath droplets. (*A*) Single frame of a 120-fps video recording of exhaled breath, crossing a 0.7-mm-thick sheet of blue laser light. Particles have undergone nucleated condensation, resulting in droplet sizes of ca. 1 to 2 μm. (*B*) Particle count as a function of frame number. The integral of the number is depicted by the solid black line, with the scale marked on the right side. Because the sheet crossing time (ca. 3 ms) is shorter than the duration of a single frame, very few droplets are visible in consecutive frames. The video is available at https://doi.org/10.5281/zenodo.6131524.

inexpensive setup therefore eliminates the effect of accelerated sedimentation caused by nucleated condensation.

In brief, two nearly identical 100-L steel chambers, each with a hydrophobic coated interior surface, were used to collect the respiratory aerosols (Fig. 2). Prior to measurements, the chamber was purged with ultraclean air and filtered at 0.01 μm, and each chamber was connected to an overflow inflatable polyethylene bag to prevent pressurization of the chamber when exhaling into it. Typically, the ultrafiltered chamber air was dried to ≤1% RH, but it could be adjusted over a wide range (1 to 98%) by humidification of the purge air. A small, adjustable-speed (3 to 20 $L{\cdot}min^{-1}$) muffin fan, mounted near the center of the chamber, could be used to homogenize the chamber contents faster than achieved by thermal convection.

For chamber 1 (Fig. 2*A*), a TSI-3330 OPS samples air from the chamber at a rate of 1 $L{\cdot}min^{-1}$ and returns this air, after HEPA filtering, to the chamber. The same chamber also contains two slit windows that allow a thin sheet of bright laser light (~10 $W.cm^{-2}$) to cross the chamber (Fig. 2*A*). A camera mounted behind the chamber enables video recording of the particles that scatter light when traversing the light sheet.

The advantage of our setup is that all respiratory aerosols enter the low-humidity chamber, where even after a single, large, ca. 5-L exhalation the RH remains below ~10%. Therefore, respiratory particles rapidly dehydrate and remain airborne or fall to the bottom of the chamber prior to full evaporation of their aqueous fraction if their initial D exceeds ca. 80 μm (40–42). Dehydrated particles larger than ca. 20 μm mostly escape detection by the OPS because they settle to the bottom of the chamber in less than a minute.

Such larger particles are readily observed in a second detection chamber that uses a 13-mm-thick, horizontal light sheet of low optical power (~0.1 $W.cm^{-2}$) passing through it, just above the floor of the chamber (Fig. 2*B*). With scattered light detected by a camera mounted on top of the chamber, ca. 60 cm above the light sheet, detection sensitivity is much reduced with this arrangement, and only particles with $D \gtrsim 4$ μm are observable.

Observation of Large Particles by Light Scattering. Using the second chamber (Fig. 2*B*), we searched for sounds that generate many droplets, confirming that the "p" sound is particularly productive. This finding agrees with historic photography by Wells (43) and more recent high-speed video recordings that show how "p" droplets originate from films and filaments that form when two wetted surfaces, the lips, are parted (44). For most subsequent measurements, we therefore used the word "popeye," where the two "p" sounds generate the droplets and the "eye" provides the requisite puff of air that propels the particles toward the center of the chamber.

A single, loud "popeye" generates several thousand detectable particles, i.e., with $D \gtrsim 4$ μm (Fig. 3 and Video S2). The brightness of the scattered light represents an approximate indicator for the size of the particle, but this intensity is modulated by interference effects of the scattered coherent light and would require Mie scattering theory for more quantitative analysis (31), which is not pursued here. As expected, a large burst of bright particles is observed clearly within the first few seconds (Fig. 3*A*), with their brightness negatively correlated with the time that elapses after speaking the word "popeye" (*Inset* in Fig. 3*A*). In other words, the larger and brighter particles fall fastest and are the first to cross the light sheet, with the smaller, dimmer particles arriving later. The arrival time in the light sheet, 53 cm below the speaker port, provides a measure for the average vertical velocity, which according to Stokes' law scales with ρD^2, where ρ is the particle density and D its diameter. For $D = 10$ μm and $\rho = 1.3\ g.cm^{-3}$, the Stokes velocity in air at room temperature is ca. 0.35 $cm{\cdot}s^{-1}$. Particles arriving in the light sheet within the first few seconds therefore had initial $D \gtrsim 80$ μm and have not yet fully dehydrated when crossing the light sheet.

The arrival time in the light sheet, $t - t_0$, determined from the frame number in which a particle is first observed, correlates well with the number of 8.3-ms video frames that particles can be tracked while crossing the light sheet (Fig. 3*B*), and similarly a fair correlation is observed between the arrival speed and crossing speed (Fig. 3*C*). The observation that the crossing speed is systematically lower than the speed derived from the arrival time, $t - t_0$, is attributed to partial dehydration by the time the particle reaches the sheet. Analysis of the crossing speeds indicates that these partially dehydrated aerosols are in the 30- to 100-μm range (Fig. 3*D*).

After the initial burst of particles, a gradually decreasing number of particles is observed to cross the light sheet, reflecting the decrease in concentration of dehydrated aerosols (Fig. 3*A*). The two mechanisms typically considered for this decrease are gravitational settling for particles larger than a few microns and, for smaller particles, diffusion-driven deposition on the floor, walls, and ceiling. Both of these processes are impacted by stirring and natural convection of air (45).

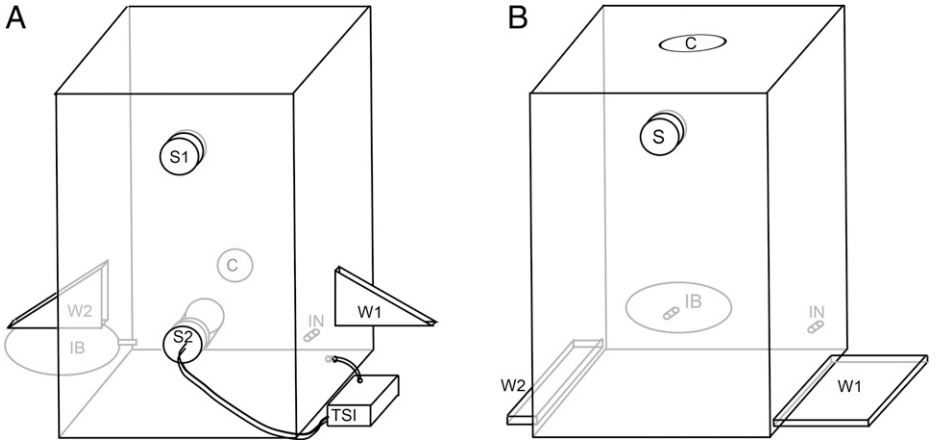

Fig. 2. Experimental arrangement for the two aerosol detection chambers. Speaker ports are labeled with S, W1 and W2 contain antireflective glass windows for the entrance and exit of laser light, C is the camera window, IB is an inflatable polyethylene bag, IN is the inlet port for ultrafiltered air, and TSI is the TSI-3330 optical particle counter. The laser light polarization is (*A*) vertical and (*B*) horizontal. For chamber 1 (*A*), a highly focused sheet (0.7-mm thickness; ~10 W.cm^{-2}) is used, and laser windows W1 and W2 are tilted at Brewster's angle relative to the light direction. For chamber 2 (*B*), the 13-mm-thick light sheet covers nearly the entire floor of the chamber and is of lower optical power density, ca. 0.1 W.cm^{-2}.

Multiple fairly bright particles are observed for tens of seconds after their initial injection into the chamber (Fig. 3*A*), indicating that convective air currents resulting from the injection of warm speech air into the room-temperature chamber can interfere with sedimentation. Modeling the effect of convection on both gravitational and diffusional deposition is complex (46, 47). However, considering that the dilution of small, $\lesssim$4 μm, aerosols in practice is dominated by the rate of ventilation, we only focus on the effect of convection on gravitational settling.

In a simplistic model, convection gives rise to uniform mixing in the chamber except for a thin boundary surface layer (47). Because gravitational settling on the smooth walls and ceiling is negligible, only deposition on the floor of the chamber needs to be considered. In the boundary layer, of thickness δh just above the floor of the chamber, the number of particles settling per unit of time is given by

$$dC_N(t)/dt = -v\delta h C_N(\mathrm{t}), \qquad [1]$$

where v is the Stokes velocity and C_N(t) is the number concentration of particles in the boundary layer. Because the particle concentration must be continuous at the junction between the boundary layer and the mixed contents, C_N(t) decreases exponentially:

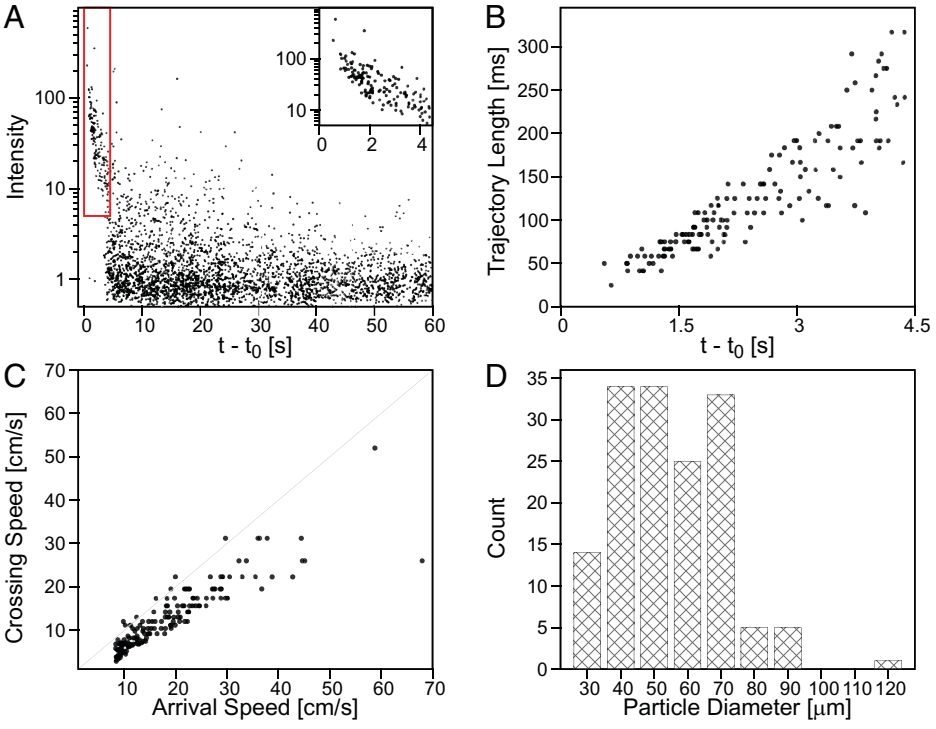

Fig. 3. Analysis of a light scattering video recording of particles generated by speaking a single word, "popeye," into chamber 2. (*A*) Integrated intensity of individual particles as a function of time, $t - t_0$, after the first "p." For each particle, its trajectory while crossing the 13-mm-thick light sheet is identified, and the reported intensity corresponds to the frame with the highest integrated value. The *Inset* shows the expanded region of the first 4.5 s, marked by the red box. (*B*) Relation between the observed trajectory length and the arrival time in the light sheet. (*C*) Correlation between the sheet crossing speed derived from the trajectory length and the arrival speed, derived from $t - t_0$ and the 53-cm vertical distance between the speaker port and the light sheet. (*D*) Size distribution of partially hydrated particles derived from crossing speeds. Video recordings can be accessed at https://doi.org/10.5281/zenodo.6131524.

$$C_N(\mathrm{t}) = C_N(0)\ \exp(-v\ t/H), \qquad [2]$$

where H is the ceiling height of the chamber. Hence, in its simplest form, an exponential decrease with time of the concentration of particles is expected, where the decay constant for particles of a given size scales with their Stokes velocity, i.e., with the square of their diameter. This result is in qualitative agreement with the decrease in brightness of particles observed during the first minute after the speech droplets enter into the chamber, i.e., the largest particles settle first and are no longer observable by light scattering (Fig. 3).

Particle Settling Rates from an Optical Particle Counter. Whereas Fig. 3*A* shows more than 100 bright particles that cross the light sheet and sediment to the floor of the chamber during the first few seconds, it also highlights the presence of a much larger abundance of particles that remain airborne. This latter, inhalable fraction is increasingly held responsible for virus transmission (48–50). When generated outdoors, particles will rapidly disperse in the atmosphere due to air currents. By contrast, indoor dispersion is restricted to the enclosed space, with the concentration of pathogens steadily increasing the longer an infected person speaks or breathes. This is consistent with the observation that outdoor transmission of respiratory virus is far less prevalent than indoor transmission (51). Quantitative analysis of particle sizes and numbers of the airborne fraction observed with the above camera system requires labor-intensive image analysis and is challenging due to Mie scattering effects. Instead, we siphoned a small fraction (~1%/minute) of the airborne, dehydrated contents of the chamber through an OPS for sizing and concentration measurements, with the air routed back into the chamber after HEPA filtering. The small loss in particle concentration resulting from the HEPA filtering is easily accounted for. The TSI-3330 OPS used in our work reports particle counts for bin sizes that are adjustable over the 0.3- to 10-μm range, plus an additional bin for particles > 10 μm.

Following the initial entry of speech aerosol, generated by 10 rapid repeats of the word "popeye," the OPS is used to monitor the decay in aerosols as a function of time and particle size inside the sealed chamber (Fig. 4*A*). Whereas virtually no decay is observed within the first half-hour for particles smaller than ~2 μm, the decay for larger aerosols follows the exponential profile of Eq. **2**. As anticipated by Stokes' law, for particles $\gtrsim$ 5 μm, the apparent gravitational settling velocity, v, scales linearly with the square of the particle diameter, with best agreement for a particle density of 1.2 g.cm^{-3} (Fig. 4*B*). The concentration of smaller aerosols decreases faster with time than predicted by gravitational sedimentation, most likely due to convection effects that facilitate their deposition on surfaces, in particular for particles that carry a small charge and can deposit electrostatically on the walls of the chamber (46, 47).

Whereas Eq. **2** predicts an inverse relation between ceiling height and sedimentation rate, this relation is usually not accounted for in modeling studies of airborne virus transmission. Here, we experimentally verify this relation by repeating the measurements in a chamber of twice the original height. As predicted by Eq. **2**, for particles $\gtrsim$ 5 μm, the sedimentation rates decrease about twofold upon doubling the chamber ceiling height to 132 cm (Fig. 4*B*). Concentrations of the smaller aerosols decrease at comparable rates when doubling the ceiling height, consistent with a dominant contribution of electrostatic diffusion deposition on the walls of the chamber, which scale linearly with the height of the chamber and have a nearly 14 times larger surface area than the floor.

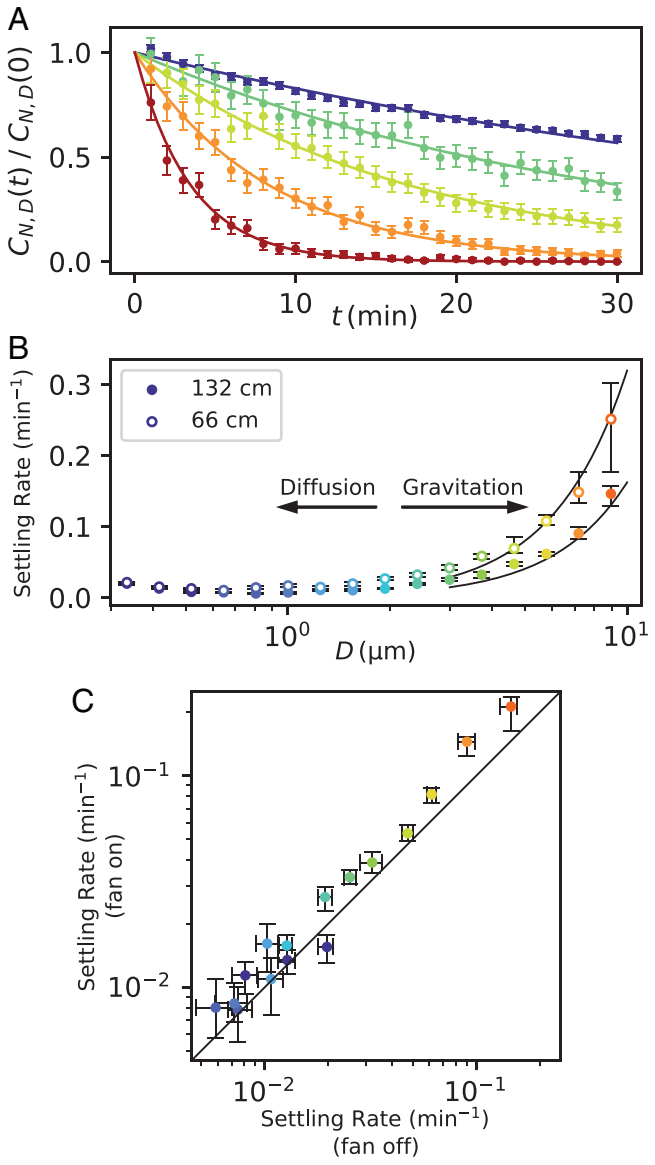

Fig. 4. Sedimentation of speech particles. (*A*) Time dependence of the normalized concentration, $C_{N,D}(t)/C_{N,D}(0)$, of speech particles of diameter D in the standard-height (66 cm) chamber after speaking 10 "popeye" words. Blue circle, 0.3 < D < 2.7 μm; green circle, 2.7 < D < 4.2 μm; yellow circle, 4.2 < D < 6.5 μm; orange circle, 6.5 < D < 10 μm; red circle, $D \geq$ 10 μm. Error bars represent 95% confidence intervals assuming the dominant source of error is Poisson noise. (*B*) Relation between sedimentation rates, $v(D)/H$, for ceiling heights, H, of 66 cm (hollow circle) and 132 cm (filled circle). The solid lines correspond to the sedimentation rates calculated from Stokes' law at 20 °C for spherical particles with a density of 1.2 g.cm^{-3} (40). (*C*) Comparison of sedimentation rates, $v(D)/H$, of aerosols in the double-height chamber in the presence and absence of stirring of the chamber air by a muffin fan operating at ca. 3 L·min^{-1}. Error bars in *B* and *C* contain 95% of settling rate estimates obtained from regression with 4096-fold non-parametric bootstrap resampling of the data.

Strong thermal gradients are present in the chamber immediately following a burst of warm, expired air. As in our earlier study (52), a small fan was used to first homogenize the contents of the chamber for ca. 20 s, prior to the start of OPS measurements. Residual convection and the small (1 L·min^{-1}) flow of air to and from the OPS then sufficed to keep the contents homogenous on longer timescales. As expected (46, 47), leaving the muffin fan running at a low speed (ca. 3 L·min^{-1}) during the entire half-hour of OPS detection slightly accelerated the particle settling rates (Fig. 4*C*), but for all quantitative measurements reported above, the fan was turned off ca. 20 s after the last spoken word, and the OPS was started 10 s later.

Breath- and Vowel-Generated Aerosols. The size distribution of particles generated by a given respiratory activity was obtained by OPS sampling of the chamber contents after the end of the activity. Knowing the sedimentation velocities, v_D, for particles of diameter D (cf. Fig. 4*A*), the concentration of breath particles of diameter D expired at time 0, $C_{N,D}(0)$, is obtained from the total number of particles, $N_D(T)$, collected in the corresponding bin during the total sampling interval, T (10 or 15 min):

$$C_{N,D}(0) = (100/V)N_D(T)(60v_D/H + 0.01)/\{1 - \exp[-T(60v_D/H + 0.01)]\}, \quad [3]$$

where V is the volume of expired air, $100/V$ is the dilution factor after mixing with the chamber contents, $60v_D/H$ is the experimentally fitted sedimentation rate in units of reciprocal minutes, 0.01 represents the effect of recirculating HEPA-filtered air (1 L·min^{-1}) back into the 100 L-chamber by the OPS, and T is the duration of OPS sampling in minutes at 1 L·min^{-1}. The volume, V, of expired air was derived from the observed increase in humidity in the chamber (27, 53). With the OPS sampling 1 L·min^{-1} from the chamber, $C_{N,D}(0)$ is in units of particles per liter. All measurements reported below include the settling correction of Eq. **3**.

Shallow tidal mouth breathing, corresponding to 20 ca. 0.7-L breaths taken over a duration of 2 min, results in low particle counts (Fig. 5*A*). Nearly all particles are smaller than 3.5 μm (Table 1 and Fig. 5), and gravitational settling is negligible on the timescale of our measurement. Both the number of particles per exhaled liter of breath (ca. 400) and the total volume of dehydrated breath aerosol resulting from tidal mouth breathing by our healthy volunteer were small, ca. 180 fL·L^{-1}. This total number of particles and their volume are comparable to values reported by Morawska et al. (27) and Gregson et al. (54). Using $\gamma = 3$, this breath aerosol corresponds to a liquid volume of ca. 5 pL of droplet volume per liter of exhaled air, or ca. 2.4 nL·h^{-1} for tidal breathing at a rate of 480 L·h^{-1}.

The number of breath particles emitted can increase significantly following deep exhalation and inhalation (38). For example, deep exhalation, followed by breath holding for 5 s, followed by maximum inspiration, and then expiration of 5 L of breath into the chamber increases particle counts by about 30-fold over tidal breathing (Fig. 5*A*). This result is fully consistent with prior reports (55, 56) and is widely interpreted as proof for the film-bursting mechanism of breath droplet generation. In this mechanism, surface tension can result in fluid plugs in the small airways, in particular during deep expiration when their diameter decreases. These liquid plugs break open during inspiration, generating droplets through the film-bursting mechanism (57). The size distribution of the deep exhalation maneuver shifts toward smaller sizes relative to tidal breathing (Fig. 5*A* and Table 1), but the total volume of dehydrated aerosol per liter of exhaled breath increases about 15-fold to ca. 2.7 pL·L^{-1} (Fig. 5*B*).

A loud "aah" sound, representative of droplets generated by the vocal folds, shows about a 10-fold increase in particle counts over tidal breathing, with a small shift to larger sizes (Fig. 5 *A* and *B*).

The total volume of dehydrated "aah" particles is ca. 13-fold higher than for tidal breathing (Table 1), indicative of a somewhat larger average particle size but with very few that are larger than 4 μm. Again, the reported values are in fair agreement with the coarser size distribution of vowel particles reported by Morawska et al. (27) and the results of Gregson et al. (54).

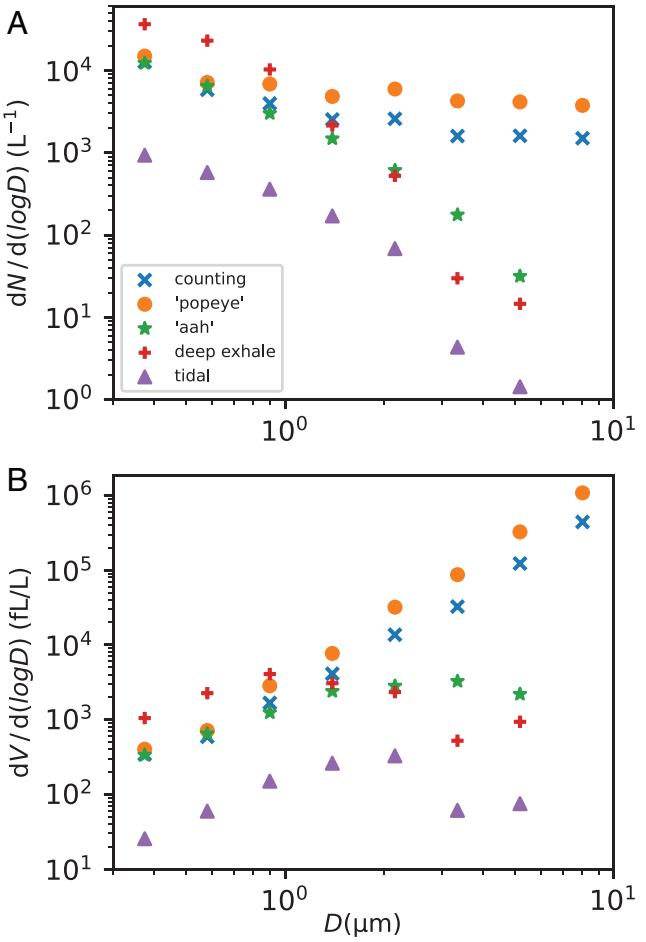

Fig. 5. Number and total volume of particles per liter of expired air during various respiratory activities, derived from Table 1. (*A*) Number of respiratory particles as a function of size for different exercises: counting 1 to 12 in a single breath (93 dB at 30 cm), repeating the word "popeye" (95 dB at 30 cm), an "aah" sound (96 dB at 30 cm), a deep exhalation maneuver (38), and tidal breathing. (*B*) Corresponding aerosol volume distribution of particles immediately after the respiratory activity.

Aerosols Generated by Speaking. In contrast to vowel sounds that produce a continuous airstream, articulation of consonants during regular speaking leads to strong modulation of the flow rate (58). We carried out two sets of measurements. First, we used the common counting exercise (2, 21, 27) but truncated it to just 12 numbers, 1 through 12, that were spoken loudly in a single breath. Even after dilution of the ca. 4 L of breath in the 100-L chamber, the counting statistics when sampling just ∼15% of its contents are excellent and give an accurate representation of the size distribution of the dehydrated aerosols (Fig. 5*A*). Clearly, the size profile is nearly flat across the entire 0.3- to 10-μm range, which corresponds to a very large increase in mass at the upper end of this size range (Fig. 5*B*).

The "p" sound is particularly effective at generating speech droplets (43), but it was absent from most prior droplet measurement studies, which relied on counting in the English language. We therefore also used five loud "popeye" repeats, spoken in a single breath, to evaluate the number of aerosols resulting from this droplet-prolific word. Indeed, we observed higher levels of aerosols across the entire size spectrum with the "popeye" repeats than with counting in English (Fig. 5*A*). Whereas the particle count values for small (≤1 μm) aerosols formed by "popeye" repeats are comparable to those of "aah" vocalization, the counts for particles ≳ 2 μm are nearly flat across the entire size range from 1 to 10 μm (Fig. 5*A*), resulting

Table 1. No. and total dry volume, *V*, of aerosols per liter of exhaled breath during various respiratory activities

	Tidal breathing		Deep exhalation		"Aah" vowel		Loud counting		Loud "popeye"	
Bin range (μm)	No. (L^{-1})	*V* (pL·L^{-1})	No. (L^{-1})	*V* (pL·L^{-1})	No. (L^{-1})	*V* (pL·L^{-1})	No. (L^{-1})	*V* (pL·L^{-1})	No. (L^{-1})	*V* (pL·L^{-1})
0.3–0.47	177	0.006	6,932	0.19	2,333	0.06	2,411	0.06	2,845	0.08
0.47–0.72	110	0.01	4,395	0.43	1,230	0.12	1,111	0.11	1,363	0.14
0.72–1.12	69	0.03	1,959	0.78	572	0.24	755	0.32	1,303	0.54
1.12–1.73	33	0.05	409	0.59	283	0.46	485	0.79	922	1.47
1.73–2.69	13	0.06	100	0.44	116	0.54	493	2.61	1,134	6.11
2.69–4.16	0.8	0.012	6	0.1	33	0.62	302	6.18	810	16.6
4.16–6.45	0.3	0.016	3.4	0.18	6	0.42	309	23.6	795	62.4
6.45–10.0	0	0	0	0	0	0	286	84.2	717	206
10–20	0	0	0	0	0	0	283	348	416	510

in an enormous increase in the airborne mass of particles at the upper end of our size range (Fig. 5*B* and Table 1).

Little variability (≤ ±25%) in the number of droplets was observed when measurements were repeated within an hour, but differences as large as 10-fold were observed when repeated far apart. Notably, a sharp increase in the number of speech droplets was observed after the consumption of a small apple. This repeatable observation suggests that the number of speech droplets may vary strongly with the composition of the oral fluid and the dryness of the lips. Results presented in Table 1 are for sets of three to five measurements, separated by less than a few hours and close to the median of all observations that spanned many months. These data highlight the large volume of speech aerosols in the ≥6.5-μm range.

Airborne Infectious Mass. The infectious airborne mass of particles, generated at time 0, decreases with time due to loss of pathogen viability, ventilation, and sedimentation. Assuming that upon inhalation the probability of acquiring an infection scales linearly with the volume of the dehydrated particle, the infection probability, $I(D)$, can be written as a proportionality (59, 60):

$$I(D) \propto D^{3/}(\alpha + \beta + v/H), \quad [4]$$

where α is the ventilation rate in units of air changes per hour, β is the decay rate for virus viability, and v/H is the sedimentation rate (cf. Eq. 2), which for $D \gtrsim 4$ μm scales with D^2 (Fig. 4*B*). A plot of the product of the mass of an aerosol and the time it stays airborne versus D (Fig. 6*A*) then shows that at small D, ≲4 μm, this product scales with the third power of D due to its cubic relation to volume, whereas at large D (≳30 μm), it scales linearly with D because the increase in volume is largely offset by its faster sedimentation, which increases with D^2. Whereas an airborne large particle carries a higher pathogen load than a small particle, the number of small particles is far higher. Therefore, to evaluate the importance of particle size on infection probability, it is important to consider Eq. **4** in the context of experimentally measured particle size distributions.

Assuming the commonly used well-mixed room model (41, 59, 60) with a modest ventilation rate, $\alpha = 2\ h^{-1}$, and a slow virus viability decay rate, $\beta = 1\ h^{-1}$, we can estimate the virus distribution as a function of aerosol size, following entry of an infected person into a 50-m^3 room with a 2.5-m ceiling height. Calculations include continuous tidal breathing and speaking a single "popeye" plus generating a vowel sound (1 L) once every 3 min. Contributions from each type of activity are shown separately (Fig. 6*B*). The distributions closely reflect those of the corresponding aerosols at the time they are generated because the decrease in concentration of infectious particles

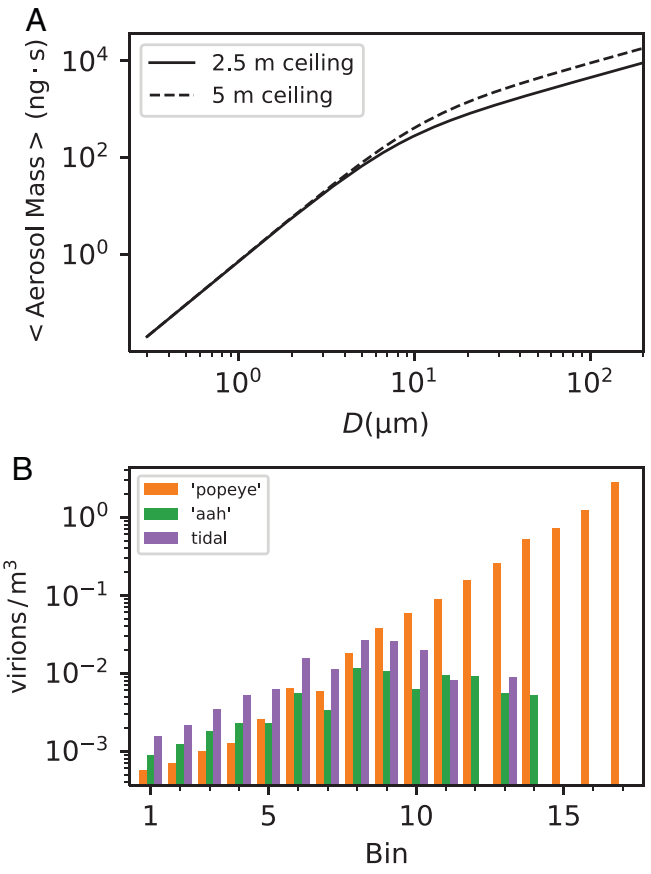

Fig. 6. Lifetime-weighted infectious respiratory aerosol mass. (*A*) Product of the mass and airborne lifetime for a single aerosol as a function of its diameter. The lifetime follows Eq. 4 for a ventilation rate of two air changes per hour and a virus viability decay constant of 1 h^{-1}. Sedimentation rates follow Stokes' law for 2.5- and 5-m ceiling heights and a particle density of 1.2 g.cm^{-3} (cf. Eq. 2). (*B*) Virus concentration for binned aerosol sizes, averaged over 1 h, assuming the originating fluid contains 7×10^6 virions per cubic centimeter and a nonvolatile matter fraction of 2%. Concentrations are averaged over 1 h, after an infected person enters a 50-m^3 room (2.5-m ceiling). Values originating from different respiratory activities are displayed: continuous tidal breathing (480 L·h^{-1}), periodic (20 h^{-1}) injection of a 1-L vowel (aah) breath, and loudly speaking a single "popeye" (0.5 L) 20 times per hour, with aerosol concentrations taken from Table 1, ignoring particles ≥ 20 μm. Bin n corresponds to the size range of (0.3 to 0.374) × 1.245^{n-1} μm. Bin 17 corresponds to particles detected by the OPS but too large (>10 μm) for sizing. Their average mass of 1.5 ng per particle is estimated from their sedimentation rate (Fig. 4*A*).

is dominated by ventilation and viability decay rates, i.e., $(\alpha + \beta) \gg v/H$. Only a moderate decrease of the importance of the largest "popeye" aerosols is seen (Fig. 6*B*) compared to their initial volume distribution. Although sedimentation becomes significant and decreases the relative importance of the largest particles, this effect is only pronounced for aerosols $\geq$ 20 μm when the airborne lifetime is less than a few minutes.

A better view of the relative contributions of respiratory activities to the airborne infectious mass is obtained by comparing aerosols generated by an infected person entering the same room at time 0, breathing at a rate of 8 L·min^{-1}, and speaking a single, loud "popeye" once every 15 min. Again, the size distributions and numbers of droplets generated by breathing and speaking are taken from our experimental measurements (Fig. 5), and we distinguish fine and coarse aerosols, where the latter can only deposit in the URT (11, 12). In this scenario, the brief speech events generate large bursts of coarse aerosols that decay about 10-fold in 15 min due to gravitational settling of the largest particles (Fig. 7). By contrast, virus in breath aerosols and the fine-aerosol "popeye" fraction increase over time until reaching a steady state, where the influx of new particles approaches the rate of depletion by ventilation (Fig. 7). As can be seen, the airborne mass generated by speaking just four words over the duration of an hour is nearly an order of magnitude larger than that generated by continuous breathing.

Our analysis neglects the impact of particles for which $D \gtrsim$ 20 μm. Such particles sediment too rapidly in our low-ceiling chambers to be measured by the OPS. However, their airborne lifetime scales roughly linearly with ceiling height and it is likely that in real-life settings, those with high ceilings and sufficient stirring of the air, such larger particles can make a significant contribution to the total aerosol burden.

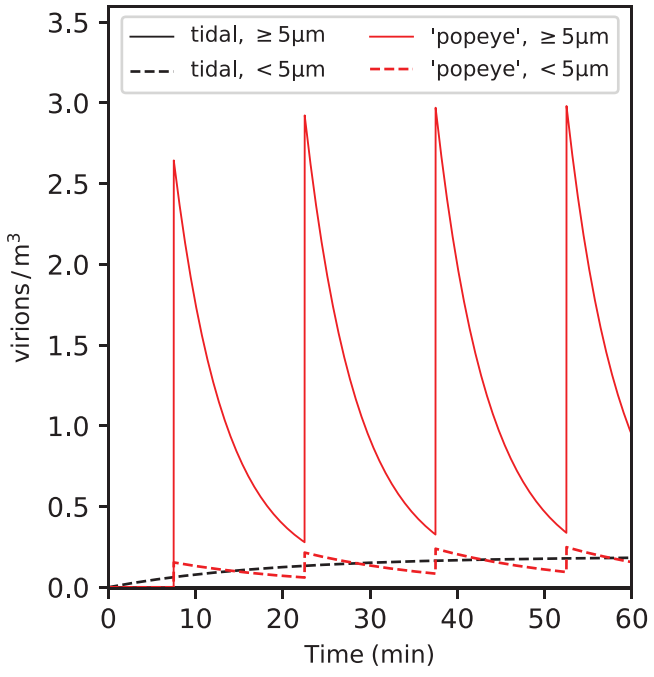

Fig. 7. Airborne virus concentration generated by a person breathing and speaking. Graphs correspond to one person entering a 50-m^3 room while tidal breathing (black) at a rate of 480 L·h^{-1} and loudly speaking the word "popeye" (0.5-L exhalation) once every 15 min (red). Calculations are for losses due to air turnover (2 h^{-1}), but neglecting the smaller effect of virus viability decay, and are for 7×10^6 virions per cubic centimeter in the fluid from which the aerosol derives. Graphs correspond to the particle size distribution of Fig. 5 and Table 1. The solid black line for larger tidal breathing particles is merged with the baseline.

Discussion

Efficacious mitigation strategies and accurate modeling of respiratory disease transmission require accurate data for the size and quantity of respiratory aerosols across the entire range. However, most important are those that do not immediately sediment prior to dehydration. Both interferometric Mie imaging (26, 31) and holographic imaging (26, 31) offer unique opportunities to view any droplet larger than a few microns directly at the mouth opening. However, practical difficulties in capturing the narrow jet of respiratory air into the small viewing window of the camera were reported to introduce large uncertainties in the total number counts (26, 31). Our approach enters all respiratory droplets directly into the low-humidity chamber. Larger droplets, $\gtrsim$80 μm, that do not fully dehydrate and fall to the bottom within the first few seconds are viewed by laser light scattering and sized based on their Stokes sedimentation velocity (Fig. 3). More important are droplets that start out $\lesssim$80 μm and that fully dehydrate prior to gravitational settling. Their numbers, sizes, and settling rates are then accurately measured by an OPS. A disadvantage of our method is that the temporal component, which correlates particles to specific sounds, is lost because OPS sampling lasts for minutes after the particles have entered the chamber.

Our measurements revealed an abundance of particles in the 5- to 20-μm range. These coarse aerosols stayed afloat for minutes and dominated the airborne mass fraction (Fig. 6). Such intermediate-sized particles are implicated in the Marin County elementary school superspreader event, where an infected teacher removed their mask while reading to the class (61). The attack rate of students seated in the two rows closest to the teacher's desk was 80%, versus 28% in the three back rows. The strong spatial gradient in attack rate points to a decrease in airborne pathogen concentration with increasing distance from the index case, as expected for aerosols that have gravitational settling rates of only a few minutes. In all cases, students were well beyond the 6-foot distance often associated with droplet transmission (62). The attack rate was high despite adequate ventilation: the classroom door and windows on opposing walls were left open, with breezy weather conditions for Marin County on the most likely day transmission took place (May 19, 2021), as well as the preceding day and following day.

While our values for breathing- and vowel-generated particles are comparable to prior measurements, we find far higher speech aerosol numbers for particles $\gtrsim$ 3 μm than prior studies (27, 35, 54, 63). The dichotomy between these APS-based measurements and our earlier laser light scattering observations (32, 52) was noted to strongly impact the modeled risk of virus exposure associated with respiratory events (41). Strikingly, high-quality light scattering observations by Alsved et al. (35) also showed an abundance of bright speech particles, but APS measurements in the same study found none larger than 4 μm. Asadi et al. (63) concluded that particle emission rates, measured by an APS, positively correlated with vowel content and that the word "papa" produced very few aerosol particles, in stark contrast with our prior and present measurements and those by others (44).

The APS and other particle counter measurements typically guide speech air and its particles through a funnel and a hose toward the APS detector, a setup that involves minimal losses when dealing with small particles in a low-humidity atmosphere (64). However, far larger losses may be expected when transporting droplets in a supersaturated atmosphere where they will rapidly grow, as shown for expired breath cooled down to room temperature (Fig. 1).

The decrease with time of the ≥4-μm aerosol concentration, observed in our chamber, correlates well with the expected sedimentation velocities of the various particle sizes (Fig. 4). This relation then allows interpretation of the OPS ≥ 10-μm overflow bin as having a geometric mean diameter of ∼13.3 μm. It is a limitation of our experimental setup that even larger particles, which sediment too fast for counting by the OPS, remain undetected. However, our light scattering arrangement highlights the presence and approximate size and volumes of such particles (Fig. 3).

Whereas the reopening of transiently closed small airways is widely considered to be the dominant mechanism for generating breath droplets (38), measurements on the effect of surface tension in the airways of anesthetized bull calves revealed additional mechanisms that involve turbulent dislodging of ALF in the bronchi and trachea (65). Our measurements, and most literature data taken on healthy volunteers, indicate a low total mass of breath aerosol, ca. 100 $ng{\cdot}h^{-1}$. Prior to dehydration, this corresponds to 1 to 5 μg of ALF, depending on its nonvolatile fraction (26, 28), or 1 to 5 $nL{\cdot}h^{-1}$ of breathing. For a viral load of 7×10^6 virions per cubic centimeter (18), many of which will not be viable, these values appear to be too low to be responsible for the high airborne contagion by asymptomatic carriers seen for SARS-CoV-2. However, it is likely that in patients with an active infection of the bronchi or small airways, inflammation will lead to swelling, which may promote the transient airway closure mechanism precisely at those locations where virus sheds (66). Indeed, a strong elevation in breath aerosol was observed for macaques when infected with SARS-CoV-2 (67), and high viral counts in the breath condensate of hospitalized patients (68) appear to be incompatible with the low quantity of breath aerosol seen in healthy people.

In a room occupied by people, and therefore containing substantial temperature gradients, the vertical component of air currents invariably is at least a few centimeters per second; i.e., it exceeds the Stokes velocity of aerosol particles smaller than ∼25 μm. Such aerosols therefore will mix across the entire vertical dimension of the room. Theory predicts, and our experiments confirm, that the rate of sedimentation correlates negatively with ceiling height (cf. Eq. 2). This slower sedimentation therefore counteracts the effect of greater dilution of the respiratory aerosol, which scales with room volume and therefore with ceiling height. It is conceivable that such high ceilings, combined with relatively low ventilation, may be one of the confounding factors contributing to substantial disease transmission rates noted in ice rinks and other sports facilities (69).

Modeling analyses of well-documented superspreader events have linked the approximately known number of virions in respiratory fluid to the attack rate in susceptible persons as a function of duration of exposure, physical activity, ventilation, and other factors (41, 59, 70). The virus-containing aerosol mass, based on past particle counter measurements, mostly lacked the dominant coarse-aerosol fraction. These modeling calculations then were consistent with observed infection rates only when assuming very high probabilities of 1 to 10% for an individual inhaled virion to result in a new infection. Although deep genome sequencing has shown that in most cases a single virion is responsible for disease transmission (71), the probability that an inhaled virion successfully invades a new host and creates progeny is very low: A recent study found that 53% of healthy human volunteers became infected upon nasal inoculation with 10 $TCID_{50}$ units (72), where $TCID_{50}$ refers to the tissue culture infectious dose, equivalent to $\sim 10^4$ RNA copies (73).This ca. 1,000-fold discrepancy between the infection probability of individual virions, obtained from the modeling results and from the human challenge study, is strongly reduced when including the large airborne mass fraction of coarse aerosol observed in our measurements.

Our study has several important implications. First, our observation that the airborne mass of coarse speech aerosol, which cannot penetrate the LRT, is nearly two orders of magnitude larger than that of fine aerosol is consistent with the observation that the vast majority of SARS-CoV-2 infections starts out in the URT. Importantly, virus-containing breath aerosol, likely to be prevalent in hospital wards occupied by COVID-19 patients with viral pneumonia, is smaller than 5 μm (Fig. 5). This fine aerosol can enter the lungs and may be linked to the high death rates among medical personnel during the early phase of the pandemic, before the use of high-quality respirators became widespread (74).

Second, even though breathing is a continuous activity, our analysis shows that the aerosol mass generated by speaking just a few words per hour can be far larger than that generated by breathing (Fig. 7). Breath particles originate in the lungs and will only contain virus if the infection involves the LRT, which is usually accompanied by symptoms. Most asymptomatic transmission therefore involves carriers with infections of the URT, where speaking represents the dominant mechanism for generating virus-containing aerosols. Such speech aerosols can be transported over considerable distances in conical, jet-like flows before dispersing in the atmosphere (58). The importance of speech droplets in SARS-CoV-2 transmission is highlighted by a review of documented superspreader events (75), with the vast majority found in places such as bars, restaurants, conferences, and cocktail receptions, all of which involve loud speech, and none reported for movie theaters or libraries, where speech activity is minimal (76). The high viral loads identified in saliva (77), in particular prior to the onset of symptoms (72), are consistent with the importance of speech aerosols in transmission of SARS-CoV-2 and suggest that reducing the concentration of viable virus in saliva may be effective at curbing transmission (78).

Third, the relatively rapid gravitational sedimentation of coarse aerosol, on the timescale of minutes (Fig. 7), poses challenges to the mitigation of virus transmission by increased ventilation. On the other hand, ventilation will effectively reduce the concentration of speech and breath fine aerosol that poses the greatest risk of severe disease.

Concluding Remarks

A proper, quantitative understanding of the size distribution of respiratory droplets forms the basis for all efforts at quantitative modeling of airborne virus transmission (41, 59, 60, 70, 79, 80). Our results suggest that the quantity of speech aerosol, in particular in the $\gtrsim$4-μm range, may have been strongly underestimated in many prior reports. The experimental setup used in our work is simple, inexpensive, and essentially loss-free for particles that fully dehydrate prior to sedimentation in the dehydration chamber, i.e., particles smaller than ca. 80 μm in their original, fully hydrated state. We hope that our findings will stimulate new research to obtain a better quantitative understanding of speech aerosols as generated in real-life settings, and their role in transmission of infectious respiratory diseases.

Materials and Methods

All measurements of respiratory droplets were carried out for a single volunteer under an exemption from the Institutional Review Board of the NIH. The OPS used for our work (TSI-3330; TSI, Shoreview, MN) was factory calibrated prior to measurements. Background counts typically were $\leq 2\ L^{-1}$. Background counts including

opening the speaker port, positioning the mouth, and closing the speaker port were $\leq 5\ L^{-1}$, with all background counts corresponding to particles $\leq 0.47\ \mu m$. Measurements were carried out by breathing or speaking into one of two steel chambers, each with dimensions of $39 \times 39 \times 66$ cm (width, depth, and height) for a total volume of 100 L (Fig. 2). Most measurements were carried out in chamber 1. For details regarding the experimental setup, measurement of breath volumes, and light intensity linearization of video recordings, see *SI Appendix*.

Data Availability. Video recordings have been deposited in Zenodo (https://doi.org/10.5281/zenodo.6131524). All other study data are included in the article.

ACKNOWLEDGMENTS. We thank James L. Baber for technical support and Ines Chen, William A. Eaton, Ingrid Pufahl, and Dennis A. Torchia for valuable comments. This work was supported by the Intramural Research Program of the National Institute of Diabetes and Digestive and Kidney Diseases.

1. D. M. Musher, How contagious are common respiratory tract infections? *N. Engl. J. Med.* **348**, 1256–1266 (2003).
2. J. P. Duguid, The size and the duration of air-carriage of respiratory droplets and droplet-nuclei. *J. Hyg. (Lond.)* **44**, 471–479 (1946).
3. M. Gandhi, D. S. Yokoe, D. V. Havlir, Asymptomatic transmission, the Achilles' heel of current strategies to control Covid-19. *N. Engl. J. Med.* **382**, 2158–2160 (2020).
4. W. F. Wells, On air-borne infection–Study II droplets and droplet nuclei. *Am. J. Hyg.* **20**, 611–618 (1934).
5. N. van Doremalen *et al.*, Aerosol and surface stability of SARS-CoV-2 as compared with SARS-CoV-1. *N. Engl. J. Med.* **382**, 1564–1567 (2020).
6. M. K. Ijaz, A. H. Brunner, S. A. Sattar, R. C. Nair, C. M. Johnson-Lussenburg, Survival characteristics of airborne human coronavirus 229E. *J. Gen. Virol.* **66**, 2743–2748 (1985).
7. O. O. Adenaiye *et al.*, Infectious severe acute respiratory syndrome Coronavirus 2 (SARS-CoV-2) in exhaled aerosols and efficacy of masks during early mild infection. *Clin. Infect. Dis.* 10.1093/cid/ciab797. (2021).
8. J. Lessler *et al.*, Incubation periods of acute respiratory viral infections: A systematic review. *Lancet Infect. Dis.* **9**, 291–300 (2009).
9. J. Flint, V. R. Racaniello, G. F. Rall, T. Hatziioannou, A. M. Skalka, *Principles of Virology* (ASM Press, 2020), **vol. 2**.
10. R. Tellier, Review of aerosol transmission of influenza A virus. *Emerg. Infect. Dis.* **12**, 1657–1662 (2006).
11. J. Gralton, E. Tovey, M. L. McLaws, W. D. Rawlinson, The role of particle size in aerosolised pathogen transmission: A review. *J. Infect.* **62**, 1–13 (2011).
12. R. Tellier, Y. Li, B. J. Cowling, J. W. Tang, Recognition of aerosol transmission of infectious agents: A commentary. *BMC Infect. Dis.* **19**, 101 (2019).
13. K. P. Fennelly, Particle sizes of infectious aerosols: Implications for infection control. *Lancet Respir. Med.* **8**, 914–924 (2020).
14. Y. J. Hou *et al.*, SARS-CoV-2 reverse genetics reveals a variable infection gradient in the respiratory tract. *Cell* **182**, 429–446.e14 (2020).
15. R. P. Dickson, J. R. Erb-Downward, F. J. Martinez, G. B. Huffnagle, "The microbiome and the respiratory tract" in *Ann. Rev. Physiol.* **78**, 481–504 (2016).
16. P. Kushalnagar, C. C. Chow, A. Bax, Self-infection with speech aerosol may contribute to COVID-19 severity. *J. Intern. Med.* **290**, 1275–1277 (2021).
17. X. He *et al.*, Temporal dynamics in viral shedding and transmissibility of COVID-19. *Nat. Med.* **26**, 672–675 (2020).
18. R. Wölfel *et al.*, Virological assessment of hospitalized patients with COVID-2019. *Nature* **581**, 465–469 (2020).
19. S. A. Lauer *et al.*, The incubation period of coronavirus disease 2019 (COVID-19) From publicly reported confirmed cases: Estimation and application. *Ann. Intern. Med.* **172**, 577–582 (2020).
20. L. Jansen *et al.*, Investigation of a SARS-CoV-2 B.1.1.529 (Omicron) variant cluster–Nebraska, November-December 2021. *MMWR Morb. Mortal. Wkly. Rep.* **70**, 1782–1784 (2021).
21. R. G. Loudon, R. M. Roberts, Droplet expulsion from the respiratory tract. *Am. Rev. Respir. Dis.* **95**, 435–442 (1967).
22. R. S. Papineni, F. S. Rosenthal, The size distribution of droplets in the exhaled breath of healthy human subjects. *J. Aerosol Med.* **10**, 105–116 (1997).
23. S. Asadi *et al.*, Aerosol emission and superemission during human speech increase with voice loudness. *Sci. Rep.* **9**, 2348 (2019).
24. T. M. Peters, D. Leith, Concentration measurement and counting efficiency of the aerodynamic particle sizer 3321. *J. Aerosol Sci.* **34**, 627–634 (2003).
25. S. Shen, P. A. Jaques, Y. Zhu, M. D. Geller, C. Sioutas, Evaluation of the SMPS–APS system as a continuous monitor for measuring PM2.5, PM10 and coarse (PM2.5 — 10) concentrations. *Atmos. Environ.* **36**, 3939–3950 (2002).
26. G. Bagheri *et al.*, Exhaled particles from nanometre to millimetre and their origin in the human respiratory tract. *medRxiv* 10.1101/2021.10.01.21264333, 2021.2010.2001.21264333 (2021).
27. L. Morawska *et al.*, Size distribution and sites of origin of droplets expelled from the human respiratory tract during expiratory activities. *J. Aerosol Sci.* **40**, 256–269 (2009).
28. M. Nicas, W. W. Nazaroff, A. Hubbard, Toward understanding the risk of secondary airborne infection: Emission of respirable pathogens. *J. Occup. Environ. Hyg.* **2**, 143–154 (2005).
29. R. M. Effros *et al.*, Dilution of respiratory solutes in exhaled condensates. *Am. J. Respir. Crit. Care Med.* **165**, 663–669 (2002).
30. H. Holmgren, B. Bake, A.-C. Olin, E. Ljungström, Relation between humidity and size of exhaled particles. *J. Aerosol Med. Pulm. Drug Deliv.* **24**, 253–260 (2011).
31. C. Y. H. Chao *et al.*, Characterization of expiration air jets and droplet size distributions immediately at the mouth opening. *J. Aerosol Sci.* **40**, 122–133 (2009).
32. P. Anfinrud, V. Stadnytskyi, C. E. Bax, A. Bax, Visualizing speech-generated oral fluid droplets with laser light scattering. *N. Engl. J. Med.* **382**, 2061–2063 (2020).
33. A. Bax, C. E. Bax, V. Stadnytskyi, P. Anfinrud, SARS-CoV-2 transmission via speech-generated respiratory droplets. *Lancet Infect. Dis.* **21**, 318 (2020).
34. P. Bahl *et al.*, Droplets and aerosols generated by singing and the risk of COVID-19 for choirs. *Clin. Infect. Dis.* **72**, e639–e641 (2021).
35. M. Alsved *et al.*, Exhaled respiratory particles during singing and talking. *Aerosol Sci. Technol.* **54**, 1245–1248 (2020).
36. S. H. Smith *et al.*, Aerosol persistence in relation to possible transmission of SARS-CoV-2. *Phys. Fluids* **32**, 107108 (2020).
37. H. Holmgren, E. Ljungstrom, A. C. Almstrand, B. Bake, A. C. Olin, Size distribution of exhaled particles in the range from 0.01 to 2.0 mu m. *J. Aerosol Sci.* **41**, 439–446 (2010).
38. B. Bake, P. Larsson, G. Ljungkvist, E. Ljungström, A. C. Olin, Exhaled particles and small airways. *Respir. Res.* **20**, 8 (2019).
39. R. R. Netz, W. A. Eaton, Physics of virus transmission by speaking droplets. *Proc. Natl. Acad. Sci. U.S.A.* **117**, 25209–25211 (2020).
40. R. R. Netz, Mechanisms of airborne infection via evaporating and sedimenting droplets produced by speaking. *J. Phys. Chem. B* **124**, 7093–7101 (2020).
41. J. Wang *et al.*, Modelling the direct virus exposure risk associated with respiratory events. *J. R. Soc. Interface* **19**, 20210819 (2022).
42. F. Dalla Barba, J. Wang, F. Picano, D. Revisiting, 2-law for the evaporation of dilute droplets. *Phys. Fluids* **33**, 051701 (2021).
43. W. F. Wells, M. W. Wells, S. Mudd, Infection of air: Bacteriologic and epidemiologic factors. *Am. J. Public Health Nations Health* **29**, 863–880 (1939).
44. M. Abkarian, H. A. Stone, Stretching and break-up of saliva filaments during speech: A route for pathogen aerosolization and its potential mitigation. *Phys. Rev. Fluids* **5**, 102301 (2020).
45. J. Corner, E. D. Pendlebury, The coagulation and deposition of a stirred aerosol. *Proc. Phys. Soc. Lond. B* **64**, 645–654 (1951).
46. J. G. Crump, J. H. Seinfeld, Turbulent deposition and gravitational sedimentation of an aerosol in a vessel of arbitrary shape. *J. Aerosol Sci.* **12**, 405–415 (1981).
47. A. C. K. Lai, W. W. Nazaroff, Modeling indoor particle deposition from turbulent flow onto smooth surfaces. *J. Aerosol Sci.* **31**, 463–476 (2000).
48. K. A. Prather *et al.*, Airborne transmission of SARS-CoV-2. *Science* **370**, 303–304 (2020).
49. L. Morawska, D. K. Milton, It is time to address airborne transmission of COVID-19. *Clin. Infect. Dis.* **71**, 2311–2313 (2020).
50. R. Zhang, Y. Li, A. L. Zhang, Y. Wang, M. J. Molina, Identifying airborne transmission as the dominant route for the spread of COVID-19. *Proc. Natl. Acad. Sci. U.S.A.* **117**, 14857–14863 (2020).
51. T. C. Bulfone, M. Malekinejad, G. W. Rutherford, N. Razani, Outdoor transmission of SARS-CoV-2 and other respiratory viruses: A systematic review. *J. Infect. Dis.* **223**, 550–561 (2021).
52. V. Stadnytskyi, C. E. Bax, A. Bax, P. Anfinrud, The airborne lifetime of small speech droplets and their potential importance in SARS-CoV-2 transmission. *Proc. Natl. Acad. Sci. U.S.A.* **117**, 11875–11877 (2020).
53. J. M. Courtney, A. Bax, Hydrating the respiratory tract: An alternative explanation why masks lower severity of COVID-19. *Biophys. J.* **120**, 994–1000 (2021).
54. F. K. A. Gregson *et al.*, Comparing aerosol concentrations and particle size distributions generated by singing, speaking and breathing. *Aerosol Sci. Technol.* **55**, 681–691 (2021).
55. G. R. Johnson, L. Morawska, The mechanism of breath aerosol formation. *J. Aerosol Med. Pulm. Drug Deliv.* **22**, 229–237 (2009).
56. H. Holmgren *et al.*, Effects of breath holding at low and high lung volumes on amount of exhaled particles. *Respir. Physiol. Neurobiol.* **185**, 228–234 (2013).
57. E. J. Burger, P. Macklem, Airway closure–Demonstration by breathing 100 percent O_2 at low lung volumes and by N_2 washout. *J. Appl. Physiol.* **25**, 139 (1968).
58. M. Abkarian, S. Mendez, N. Xue, F. Yang, H. A. Stone, Speech can produce jet-like transport relevant to asymptomatic spreading of virus. *Proc. Natl. Acad. Sci. U.S.A.* **117**, 25237–25245 (2020).
59. M. Z. Bazant, J. W. M. Bush, A guideline to limit indoor airborne transmission of COVID-19. *Proc. Natl. Acad. Sci. U.S.A.* **118**, e2018995118 (2021).
60. Z. Peng *et al.*, Practical indicators for risk of airborne transmission in shared indoor environments and their application to COVID-19 outbreaks. *Environ. Sci. Technol.* **56**, 1125–1137 (2022).
61. T. Lam-Hine *et al.*, Outbreak associated with SARS-CoV-2 B.1.617.2 (Delta) variant in an elementary school–Marin County, California, May-June 2021. *MMWR Morb. Mortal. Wkly. Rep.* **70**, 1214–1219 (2021).
62. CDC, Scientific Brief: SARS-CoV-2 Transmission (2021). https://www.cdc.gov/coronavirus/2019-ncov/science/science-briefs/sars-cov-2-transmission.html. Accessed 19 February 2022.
63. S. Asadi *et al.*, Effect of voicing and articulation manner on aerosol particle emission during human speech. *PLoS One* **15**, e0227699 (2020).
64. Y. S. Cheng, C. S. Wang, Motion of particles in bends of circular pipes. *Atmos. Environ.* **15**, 301–306 (1981).
65. W. Watanabe *et al.*, Why inhaling salt water changes what we exhale. *J. Colloid Interface Sci.* **307**, 71–78 (2007).
66. J. Yan *et al.*; EMIT Consortium, Infectious virus in exhaled breath of symptomatic seasonal influenza cases from a college community. *Proc. Natl. Acad. Sci. U.S.A.* **115**, 1081–1086 (2018).
67. D. A. Edwards *et al.*, Exhaled aerosol increases with COVID-19 infection, age, and obesity. *Proc. Natl. Acad. Sci. U.S.A.* **118**, e2021830118 (2021).
68. J. Ma *et al.*, Coronavirus disease 2019 patients in earlier stages exhaled millions of severe acute respiratory syndrome coronavirus 2 per hour. *Clin. Infect. Dis.* **72**, e652–e654. (2021).
69. D. Atrubin, M. Wiese, B. Bohinc, An outbreak of COVID-19 associated with a recreational hockey game - Florida, June 2020. *MMWR Morb. Mortal. Wkly. Rep.* **69**, 1492–1493 (2020).
70. G. Buonanno, L. Morawska, L. Stabile, Quantitative assessment of the risk of airborne transmission of SARS-CoV-2 infection: Prospective and retrospective applications. *Environ. Int.* **145**, 106112 (2020).
71. M. A. Martin, K. Koelle, Comment on "Genomic epidemiology of superspreading events in Austria reveals mutational dynamics and transmission properties of SARS-CoV-2". *Sci. Transl. Med.* **13**, eabh1803 (2021).
72. B. Killingley *et al.*, Safety, tolerability and viral kinetics during SARS-CoV-2 human challenge in young adults. *Nat. Med.* 10.1038/s41591-022-01780-9. (2022).

73. R. Sender *et al.*, The total number and mass of SARS-CoV-2 virions. *Proc. Natl. Acad. Sci. U.S.A.* **118**, e2024815118 (2021).
74. P. Lapolla, A. Mingoli, R. Lee, Deaths from COVID-19 in healthcare workers in Italy-What can we learn? *Infect. Control Hosp. Epidemiol.* **42**, 364–365 (2021).
75. D. Majra, J. Benson, J. Pitts, J. Stebbing, SARS-CoV-2 (COVID-19) superspreader events. *J. Infect.* **82**, 36–40 (2021).
76. V. Stadnytskyi, P. Anfinrud, A. Bax, Breathing, speaking, coughing or sneezing: What drives transmission of SARS-CoV-2? *J. Intern. Med.* **290**, 1010–1027 (2021).
77. N. Huang *et al.*; NIH COVID-19 Autopsy Consortium; HCA Oral and Craniofacial Biological Network, SARS-CoV-2 infection of the oral cavity and saliva. *Nat. Med.* **27**, 892–903 (2021).
78. H. Daniell *et al.*, Debulking SARS-CoV-2 in saliva using angiotensin converting enzyme 2 in chewing gum to decrease oral virus transmission and infection. *Mol. Ther.* **30**, 1966–1978 (2022).
79. P. Z. Chen *et al.*, Heterogeneity in transmissibility and shedding SARS-CoV-2 via droplets and aerosols. *eLife* **10**, e65774 (2021).
80. F. Pourfattah *et al.*, Challenges in simulating and modeling the airborne virus transmission: A state-of-the-art review. *Phys. Fluids* **33**, 101302 (2021).